

Article

Microstructure, Mechanical Property, and Wear Behavior of NiAl-Based High-Entropy Alloy

Ziyan Li ¹, Xiaohong Wang ^{1,*}, Yanyan Huang ¹, Zhixin Xu ¹, Yulei Deng ¹, Xiaoying Jiang ¹ and Xiaohong Yang ^{2,3,*}

¹ Key Laboratory of Air-Driven Equipment Technology of Zhejiang Province, Quzhou University, Quzhou 324000, China; 17787520612@163.com (Z.L.); 18786192941@163.com (Y.H.); zhixinxu2022@163.com (Z.X.); 18750972225@163.com (Y.D.); qz_jxy@163.com (X.J.)

² Academician Expert Workstation, Jinhua Polytechnic, Jinhua 321017, China

³ Key Laboratory of Crop Harvesting Equipment Technology of Zhejiang Province, Jinhua 321017, China

* Correspondence: 36098@qzc.edu.cn (X.W.); jhyxh656593@163.com (X.Y.); Tel.: +86-18268975632 (X.W.); +86-13967039758 (X.Y.)

Abstract: Based on the excellent comprehensive mechanical properties of high-entropy alloy (HEA), the NiAl-based HEA was designed to achieve excellent high-temperature strength, toughness, and wear resistance. In this work, vacuum arc melting technology was used to prepare (NiAl)₇₈(CoCrFe)_{16.5}Cu_{5.5} HEA, and its microstructure, phase composition, and mechanical properties were systematically studied. The results showed that (NiAl)₇₈(CoCrFe)_{16.5}Cu_{5.5} HEA was composed of FCC and BCC/B2, with a spinodal decomposition structure in the matrix, and nano-precipitation in the interdendritic, exhibiting a good high-temperature performance. At 600 °C, the compressive fracture strength is 842.5 MPa and the fracture strain is 24.5%. When the temperature reaches 800 °C, even if the strain reaches 50%, the alloy will not fracture, and the stress-strain curve shows typical work hardening and softening characteristics. The wear coefficient of the alloy first increases and then decreases with the increase in temperature in the range of room temperature to 400 °C. However, the specific wear rate shows the opposite trend. At 100 °C, the wear rate reaches the lowest of 7.05×10^{-5} mm³/Nm, and the wear mechanism is mainly abrasive wear.

Keywords: NiAl-based high-entropy alloys; spinodal decomposition; mechanical property; wear



Citation: Li, Z.; Wang, X.; Huang, Y.; Xu, Z.; Deng, Y.; Jiang, X.; Yang, X. Microstructure, Mechanical Property, and Wear Behavior of NiAl-Based High-Entropy Alloy. *Coatings* **2023**, *13*, 1737. <https://doi.org/10.3390/coatings13101737>

Academic Editor: Elena Villa

Received: 10 September 2023

Revised: 24 September 2023

Accepted: 4 October 2023

Published: 6 October 2023



Copyright: © 2023 by the authors. Licensee MDPI, Basel, Switzerland. This article is an open access article distributed under the terms and conditions of the Creative Commons Attribution (CC BY) license (<https://creativecommons.org/licenses/by/4.0/>).

1. Introduction

High-entropy alloys (HEAs) are a rapidly developing new material that is composed of four or more elements with equal or nearly equal molar ratios [1–3]. Compared with traditional alloys, the high mixing entropy of HEAs tends to form single-phase solid solution ($\delta < 6.6$, $-15 < \Delta H_{\text{mix}} < 5$ KJ/mol, $12 < \Delta S_{\text{mix}} < 17.5$ KJ/mol) [3], inhibit the formation of intermetallic compounds, and provide excellent high-temperature mechanical and wear properties [4,5]. However, single-phase solid solutions typically do not have excellent plasticity and strength at the same time. To solve the contradiction between the strength and plasticity of single-phase HEAs, it is encouraged to relax the strict restrictions on single-phase solid solutions to achieve excellent comprehensive performance. In recent years, Lu et al. [6] proposed eutectic high-entropy alloys (EHEAs) and prepared AlCoCrFeNi_{2.1} EHEAs ingots with excellent strength and plasticity. In addition, the combination of HEAs with good strength and ductility can also be obtained by introducing nano-precipitation [7–10]. Based on this design concept, Jin et al. [11] proposed the use of the pseudo-binary method to design Al₁₇Co_{14.3}Cr_{14.3}Fe_{28.6}Ni_{25.8} EHEAs consisting of nanoscale B2 phases and FCC phases, it shows high strength (1145 MPa) and fracture toughness (10.3%). The above studies are all aimed at introducing a second phase into a single-phase matrix to improve the comprehensive performance of the HEA.

It is reported that nickel aluminum (Ni-Al) alloy has high strength, low density, low cost, and good creep resistance, and is widely used in fields such as aerospace and automotive [12–15]. NASA has also predicted the materials of future aviation generators, among

which β -NiAl intermetallic compounds have significant advantages in terms of service temperature, antioxidants, and high-temperature structural strength/lifespan. They are one of the most important and potential materials in high-temperature environments [4,5]. However, its room temperature brittleness and inadequate strength limit its industry application. Therefore, this work considers preparing NiAl-based HEAs based on β -NiAl intermetallic compounds to obtain BCC and FCC dual phase composition. Furthermore, achieved better comprehensive performance alloys. At present, a common way to improve the property is alloying NiAl (Co, Cr, Fe, Cu, Mo, Ti, and Hf), such as 52.4Ni-43.5Al-4.1Cr, 51.1Ni-42.2Al-4.1Cr-2.6Fe, 90Cr-4Ni-6Al, 82Cr-4Ni-6Al-8.0Fe [16], Ni-30Fe-20Al, Ni-30Fe-23Al, Ni-33Fe-21Al [17], Fe₂₀Co₂₀Ni₄₁Al₁₉ [18], Ni-26Al-50Co, Ni-25Al-18Fe, Ni-24Al-30Cu, Ni-20Al-20Cr [19], Al_{0.6}CoCrFeNi, Al_{1.2}CoCrFeNi [20], Ti + 10%Al_{0.6}CoCrFeNi [21], NiAl-28Cr-5.5Mo-0.5Hf(DS) [22], NiAl-12Cr-6Co [23], and NiAl-Cr(Mo)-5Fe [24]. Among these alloys, the room temperature brittleness of alloys, including Mo/Cr/Fe/Cu/Co, can be significantly improved, and the strength of alloys NiAl-Cr can be enhanced (Table 1). Based on this research, for example, the yield strength of Ni_{50.7}Al_{19.3}Co₁₅Cr₁₅ HEAs prepared by Liu et al. [15] reached 789 MPa at 600 °C; the yield strength and fracture strength of NiAl-Mo_yCr_yFe_y ($y = 13.33$) reached 1854 MPa and 3308 MPa, respectively [25].

Table 1. A brief overview of the property of NiAl alloys [16–24].

| Materials (at.%) | Yield Strength (MPa) | Compressive Strength (MPa) | Compressive Strain (%) |
|---|----------------------|----------------------------|------------------------|
| 52.4Ni-43.5Al-4.1Cr | - | 1026 ± 29 | 9.3 ± 0.5 |
| 51.1Ni-42.2Al-4.1Cr-2.6Fe | - | 1220 ± 37 | 11.8 ± 1.4 |
| 90Cr-4Ni-6Al | - | 736 ± 32 | 6.4 ± 0.7 |
| 82Cr-4Ni-6Al-8.0Fe | - | 964 ± 38 | 7.4 ± 0.3 |
| Ni-30Fe-20Al | 1065 | - | - |
| Ni-30Fe-23Al | 1120 | - | - |
| Ni-33Fe-21Al | 1150 | - | - |
| Fe ₂₀ Co ₂₀ Ni ₄₁ Al ₁₉ | 577 | 1103 | 18.7 |
| Ni-26Al-50Co | - | - | 10.2 |
| Ni-25Al-18Fe | - | - | 6.1 |
| Ni-24Al-30Cu | - | - | 0 |
| Ni-20Al-20Cr | - | - | 2.5 |
| Al _{0.6} CoCrFeNi | - | 1903.42 | 21.26 |
| Al _{1.2} CoCrFeNi | - | 1462.36 | 18.05 |
| Ti + 10% Al _{0.6} CoCrFeNi | - | 1642 | 21.7 |
| NiAl-28Cr-5.5Mo-0.5Hf(DS) | - | 255 | - |
| NiAl-12Cr-6Co | - | 1989 | 0.11 |
| NiAl-Cr(Mo)-5Fe | - | 2229 | 0.29 |

Previous studies have shown that microalloying can optimize the phase composition and microstructure of the alloys, thereby improving the mechanical properties of HEAs [26–29]. Miracle et al. [30] comprehensively evaluated experimental data from 408 different alloys using three datasets, establishing a clear relationship between the composition, microstructure, and properties of the three-dimensional transition metal, of which Cr is crucial for good strength. Meanwhile, the addition of Cu elements has the effects of grain refinement [31], and can promote the formation of wear-resistant glaze layers together with CuO to achieve high-temperature wear resistance [32]. The microstructure of CoCrCuFeNi series HEAs was studied by Gao et al. [33], it found that the Cr and Fe elements are conducive to improving the hardness of the alloy.

Therefore, the (NiAl)₇₈(CoCrFe)_{16.5}Cu_{5.5} HEAs are designed based on the NiAl binary system. Their microstructure, mechanical properties, and friction and wear properties at room and high temperatures were studied through XRD, EDS, SEM, and EBSD. It provides a new design approach for NiAl-based high-temperature alloys and promotes the high-temperature application of HEAs.

2. Experimental Procedures

Al, Co, Cr, Fe, Ni, and Cu (purity of 99.99 wt%, Beijing Dream Material Technology Co., Ltd. Beijing, China) were used as raw materials, and $(\text{NiAl})_{78}(\text{CoCrFe})_{16.5}\text{Cu}_{5.5}$ (at%) HEAs alloy ingots (100 g, collar button shape) were prepared in a vacuum arc melting furnace (DHL-500 II, solidification rate $10^2\text{--}10^5$ K/s) under a high-purity argon atmosphere. X-ray fluorescence (XRF, S2 PUMA Series II) spectrometry is applied in the determination of elemental compositions (Table 2). Each alloy ingot is re-melted five times to ensure that the alloy composition was homogeneous. The ingots were cut using wire cutting, followed by grinding and polishing. Then, the microstructure, phase composition, and chemical composition of the sample are analyzed by a scanning electron microscope (SEM, Hitachi SU8010) with an energy dispersion spectrometer (EDS) at a voltage of 15 kV. An X-ray diffraction meter (XRD, Rigaku D/max RB) was used to qualitatively analyze the crystal structure of the alloy to identify the phase composition. The radiation source is $\text{Cu-k}\alpha$ ray, the wide-angle diffraction test is $25\text{--}90^\circ$, and the test rate is $5^\circ/\text{min}$.

Table 2. The chemical composition of the $(\text{NiAl})_{78}(\text{CoCrFe})_{16.5}\text{Cu}_{5.5}$ HEAs after XRF analysis.

| | Ni | Al | Co | Cr | Fe | Cu |
|------|-------|-------|------|------|------|------|
| wt.% | 49.67 | 22.84 | 7.03 | 6.21 | 6.67 | 7.58 |
| at.% | 39 | 39 | 5.5 | 5.5 | 5.5 | 5.5 |

A compression sample with a length of 10 mm and a diameter of 6 mm was prepared by wire cutting, and the surface of the cylinder was polished to 1500 mesh with SiC sandpaper. The MTS hydraulic servo test system is used for room-temperature (25°C) and high-temperature (600°C and 800°C) compression tests (Figure 1). All samples were tested three times to obtain the average value. After the compression test, the fracture morphology and crack propagation of the alloy were observed with SEM. The electron backscatter diffraction (EBSD) under 20 Kv accelerated current to determine the relationship between microstructure and mechanical properties.

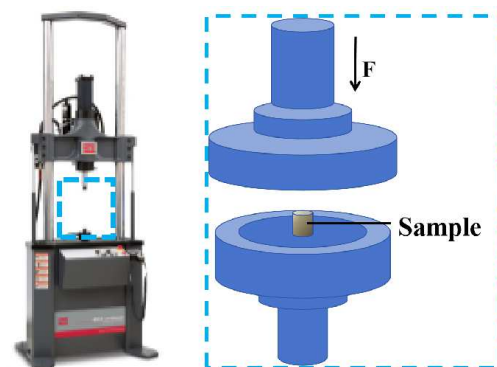


Figure 1. Compression and its local schematic diagram.

In addition, we tested the wear behaviors by a HT-1000 tribology tester (Lanzhou Zhongke Kaihua Co., Ltd. Lanzhou, China) using a Si_3N_4 ball with a size of $\Phi 4$ mm as the grinding pair. During the experiment, the parameters were set as: load 10 N, wear trajectory radius 2 mm, motor speed 600 r/min, sliding time 30 min, and temperature $25\text{--}400^\circ\text{C}$. The friction coefficient was recorded during the sliding process. After the wear test, the wear volume (W_V) was determined by KEYENCE three-dimensional surface profile measuring instrument. The morphologies and compositions of the wear scars were examined by SEM and EDS, respectively.

3. Results and Discussion

3.1. Microstructure and Phase Composition

Figure 2 shows the XRD diffraction pattern of $(\text{NiAl})_{78}(\text{CoCrFe})_{16.5}\text{Cu}_{5.5}$ HEAs. It can be seen that the alloy has two crystal structures, i.e., FCC and BCC, and it is a typical dual-phase alloy. At $2\theta = 36.8^\circ$ and 43.1° , the diffraction peaks represent the FCC phase, while the BCC phase mainly occurred at $2\theta = 44.6^\circ$, 64.9° , and 82.2° positions. In addition, the B2 phase was also detected at $\theta = 30.7^\circ$.

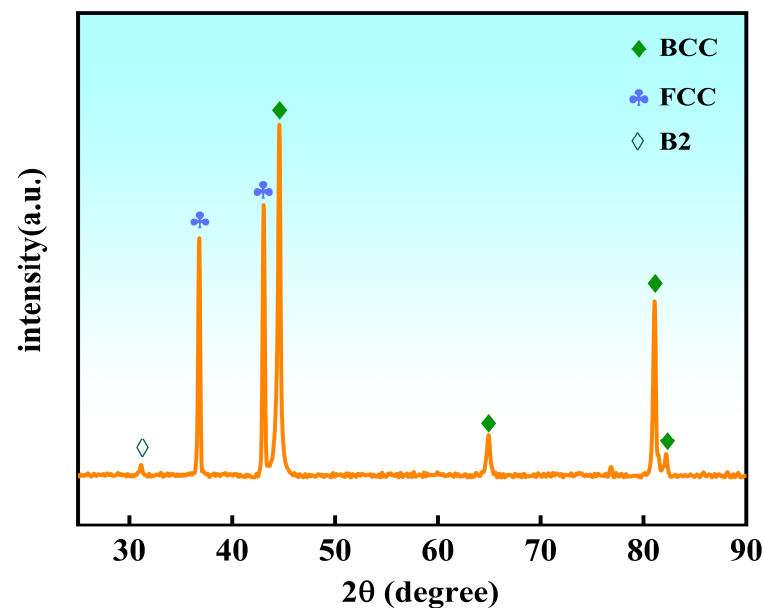


Figure 2. XRD patterns of $(\text{NiAl})_{78}(\text{CoCrFe})_{16.5}\text{Cu}_{5.5}$ HEAs.

Figure 3 shows the microstructure and map scanning results of $(\text{NiAl})_{78}(\text{CoCrFe})_{16.5}\text{Cu}_{5.5}$ HEAs. The microstructure of the alloy exhibits a typical dendritic morphology, with the gray phase distributed in the dendritic region and the white phase distributed in the interdendritic region (Figure 3a,b). Through local magnification observations (Figure 3c), it is found that the gray phase has a plate strip shape, which belongs to a typical spinodal decomposition structure. The microstructure of AlCrFeCoNiCu was studied by Ping et al. [34], which indicates that the spinodal decomposition structure was distributed alternately by the A2 phase and B2 phase. The $\text{Al}_x\text{CoCrCuFeNi}$ HEAs with different Al contents were studied by Liu Yuan et al. [35], it found that spinodal decomposition structure can improve the strength of the alloy due to its high arrangement density [36]. It can also be found from Figure 3c that there are a large number of precipitations distribution in the interdendritic. In order to further analyze the elemental distribution, EDS map scanning analysis was performed (Figure 3d), and it can be clearly observed that dendrites are enriched with Al, Co, Cr, and Fe elements, while Cu and Ni elements are enriched in the interdendritic region, which is due to the significant difference in the mixing enthalpy between Cu element and Al, Co, Cr, and Fe. The mixing enthalpy with Cr and Fe elements has exceeded 10 KJ/mol. However, the mixing enthalpy of Ni-Cu and Ni-Al is relatively small, and the binding energy of Ni element with other elements is relatively poor. At the same time, the content of Ni and Al elements is relatively high. Therefore, dendrites and interdendritic phases coexist. Based on the XRD results, it can be concluded that the structure of dendrite is BCC and the interdendritic is FCC. Furthermore, in the interdendritic, there are spherical precipitation phases which are enriched with Cr and Fe.

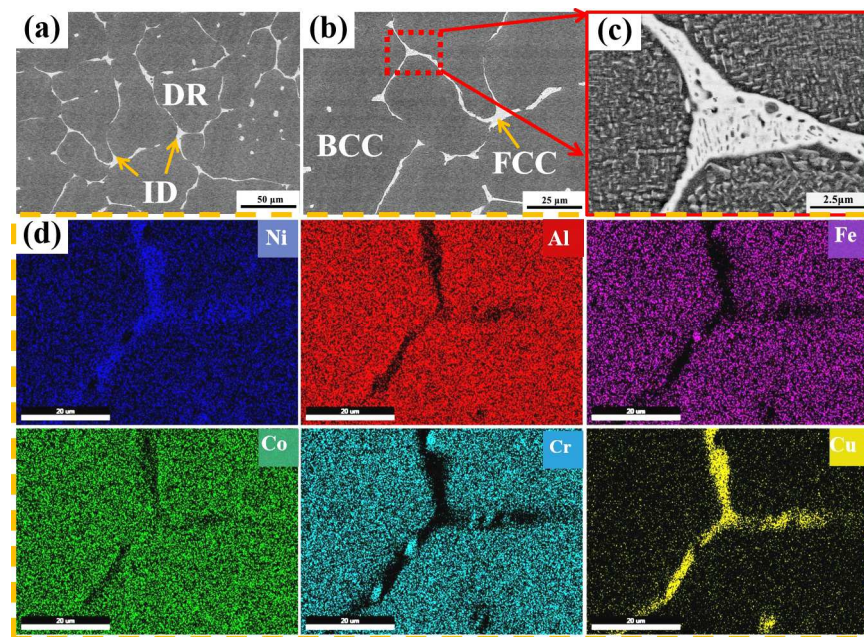


Figure 3. SEM and EDS map scanning of $(\text{NiAl})_{78}(\text{CoCrFe})_{16.5}\text{Cu}_{5.5}$ HEAs. (a–c) SEM; (d) map scanning.

3.2. Mechanical Properties

3.2.1. Compression Property

Figure 4 shows the compression stress–strain curve of $(\text{NiAl})_{78}(\text{CoCrFe})_{16.5}\text{Cu}_{5.5}$ HEAs at different temperatures and the compression fracture morphology at room temperature and 600 °C. Insets of Figure 4a,b summarize the compressive strength and strain. As shown in Figure 4a, $(\text{NiAl})_{78}(\text{CoCrFe})_{16.5}\text{Cu}_{5.5}$ HEAs have a compressive strength of 1039.9 MPa at room temperature and a fracture strain of 0.9%. When the test temperature reaches 600 and 800 °C (Figure 4b), the yield strength gradually decreases with the increase in temperature, while the fracture strain shows the opposite trend. At 600 °C, the alloy still maintains high compressive strength and exhibits good plasticity. Further increasing the test temperature to 800 °C, the sample did not fracture even under compression strain exceeding 50%, indicating that HEA has excellent high-temperature plasticity. To further analyze the relationship between compression performance and microstructure, SEM was performed on the fracture surface. The compression fracture morphology at room temperature is shown in Figure 4c,d. The fracture surface is relatively rough, containing a large number of tearing edges, which also can clearly observe river-like patterns and cracks. It indicates that the fracture mechanism of the alloy exhibits a typical quasi-cleavage fracture. Generally, only cold brittle metals can undergo cleavage fracture. Yuan et al. [36] have shown that Al plays a role of solid solution strengthening. Combined with the brittle structure of the BCC phase in XRD, higher hardness will cause a tearing effect on the matrix, when bearing the load, it is easy to form local stress concentration, which can promote the generation and propagation of cracks, leading to a decrease in the strength and elongation. From Figure 4e,f, it can be seen that the morphology of the fracture surface after high-temperature compression at 600 °C is granular, and a small number of cracks appear. According to the path of crack propagation, it indicates that the cracks have both intergranular and transgranular fractures. The main reason is that the grain boundary strength of HEAs decreases under high-temperature and high-stress environments, and the sliding and diffusion of grain boundaries are relatively sufficient, resulting in changes in the structure and strength of grain boundaries. When stress is concentrated near the grain boundary, the material at the grain boundary often softens due to creep, leading to fracture and promoting the formation and development of voids and cracks along the grain boundary.

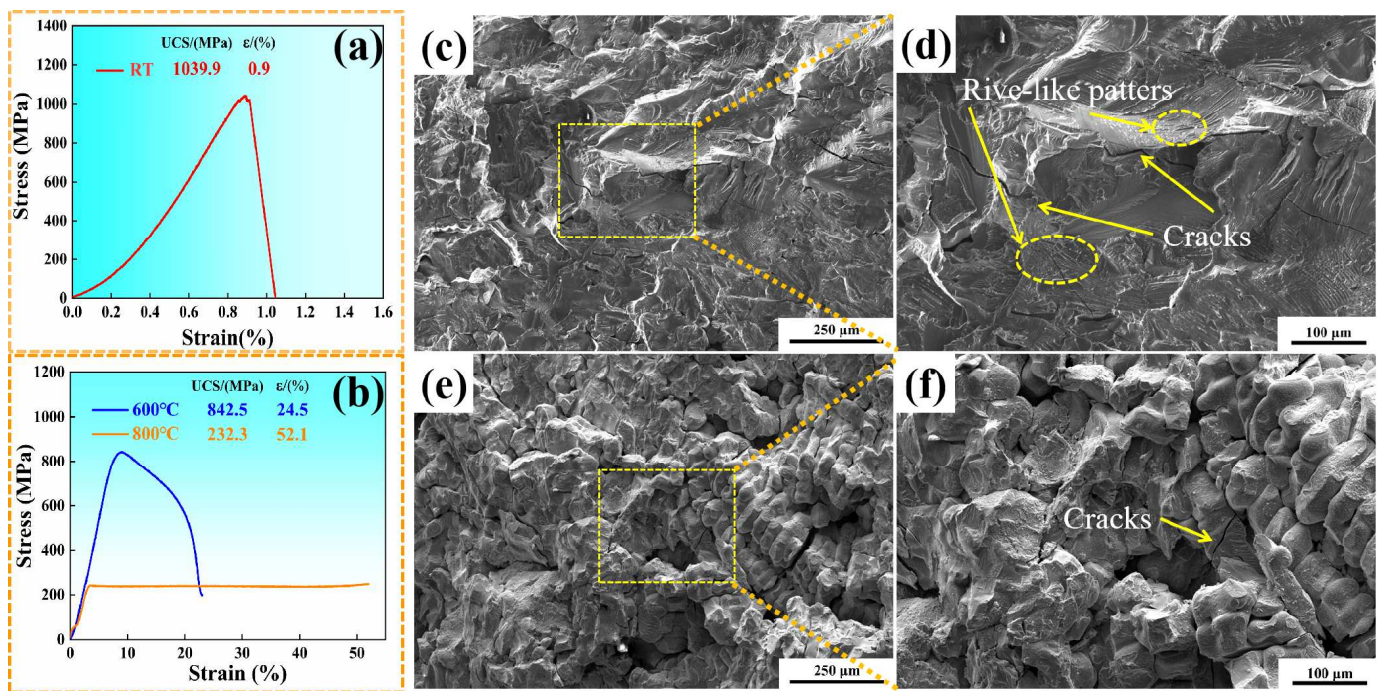


Figure 4. Compression test results of $(\text{NiAl})_{78}(\text{CoCrFe})_{16.5}\text{Cu}_{5.5}$ HEAs. Compression stress–strain curve: (a) room temperature; (b) 600 °C and 800 °C; compression fracture morphology at different temperatures: (c,d) RT; (e,f) 600 °C.

Figure 5 shows the EDS map scanning results and compression fracture after polishing of $(\text{NiAl})_{78}(\text{CoCrFe})_{16.5}\text{Cu}_{5.5}$ HEAs after compression at different temperatures. As the temperature increases, the microstructure after compression at room temperature and 600 °C exhibits both transgranular and intergranular fractures, with only intergranular fractures at 800 °C. Compared with the map scanning results in Figure 3, the Cr and Fe elements gather near the interdendritic and enrich and grow at 600 and 800 °C after compression, while the Ni elements become uniformly distributed in the dendrite. Meanwhile, the precipitations enriched in Cr and Fe in the FCC phase have grown. Furthermore, according to the SEM results, it can be seen that when transgranular cracks encounter (Cr, Fe)-rich phases, deflection occurs. The results indicate that under the effect of pressure, Cu segregation between dendrites weakens, and (Cr, Fe)-rich nano precipitates aggregate and grow into irregular blocks. When the compression temperature increases to 600 °C, the size of interdendritic (Cr, Fe)-rich phases decreases, indicating that high temperatures can promote the diffusion and homogenization of Cr and Fe elements. When the compression temperature increases to 800 °C, the precipitation of interdendritic (Cr, Fe)-rich phases gradually presents a continuous distribution between the dendrites, resulting in a decrease in intergranular bonding force and intergranular fracture under external forces.

The X-ray diffraction pattern of $(\text{NiAl})_{78}(\text{CoCrFe})_{16.5}\text{Cu}_{5.5}$ HEAs is shown in Figure 6. By comparing the XRD results after compression at room temperature and 800 °C. The results show that the $(\text{NiAl})_{78}(\text{CoCrFe})_{16.5}\text{Cu}_{5.5}$ HEAs still exhibit dual phases of BCC and FCC after 800 °C compression. However, as the temperature increases, it can be observed that the diffraction peak intensity of BCC and B2 lattices increases, while the diffraction peak intensity of FCC lattices decreases. During the hot processing of metal materials, dynamic recovery or recrystallization may occur. In order to further investigate the relationship between the microstructure and mechanical properties of $(\text{NiAl})_{78}(\text{CoCrFe})_{16.5}\text{Cu}_{5.5}$ HEAs after high-temperature compression at 800 °C, the EBSD technology was used. Figure 7 shows the reverse pole diagram (IPF diagram), DefRex diagram, local dislocation misorientation, and grain boundary distribution diagram of $(\text{NiAl})_{78}(\text{CoCrFe})_{16.5}\text{Cu}_{5.5}$ HEAs. The IPF in Figure 7a shows that there is no obvious texture formation in the compressed grain at

800 °C, and the orientation distribution is random. In the DefRex diagram, blue represents substructure, red represents deformed grains, and yellow represents recrystallized grains. As shown in Figure 7b, a small amount of subgrains and recrystallized grains appear inside the original deformed grains. In Figure 7c, it can be observed that there is severe plastic deformation in the [111] and [001] textures, resulting in a higher dislocation density. Figure 7d shows that most of the grain boundaries have a small angle, containing many deformed grains inside the material. The distribution of large-angle grain boundaries indicates that the grains also undergo dynamic recrystallization during the compression process, but the recrystallization process is incomplete and there are many original grains. The formation of substructures requires the consumption and absorption of some dislocations, while there is basically no dislocation formation inside the recrystallized grains. Recrystallization can restore the plasticity of the material, and eliminate the texture and stress generated by deformation. In addition, BCC is mostly strain-free after high-temperature compression, plastic strain is regulated by the FCC phase [37]. Based on the above analysis, it can be seen that the BCC phase can restore some strength and plasticity of the material, but usually does not completely eliminate deformation. The FCC phase can improve the uniformity of microstructure and is more effective in improving strength and toughness. Dual-phase HEAs undergo dynamic recovery and recrystallization of metal materials at higher temperatures and lower strain rates, resulting in increased strength and plasticity of the material itself. The work hardening process and dynamic softening process reach equilibrium, and finally, the stress–strain curve reaches a steady state under compression at 800 °C.

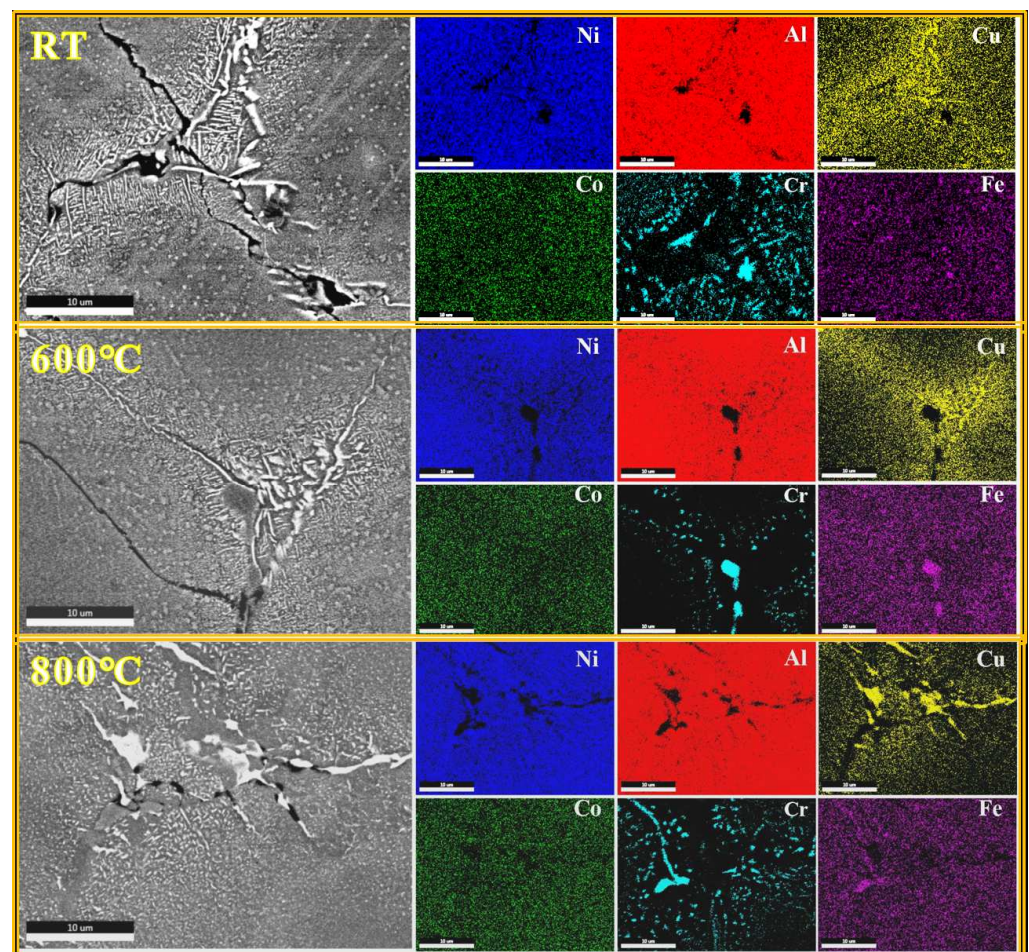


Figure 5. The SEM and EDS of compression fracture for $(\text{NiAl})_{78}(\text{CoCrFe})_{16.5}\text{Cu}_{5.5}$ HEAs.

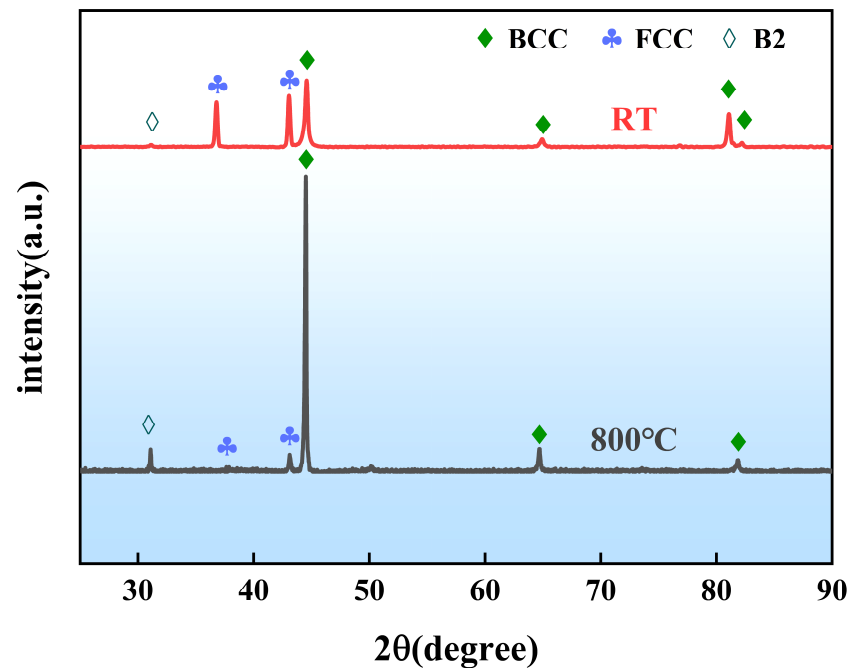


Figure 6. XRD patterns after thermal compression treatment at room temperature and 800 °C.

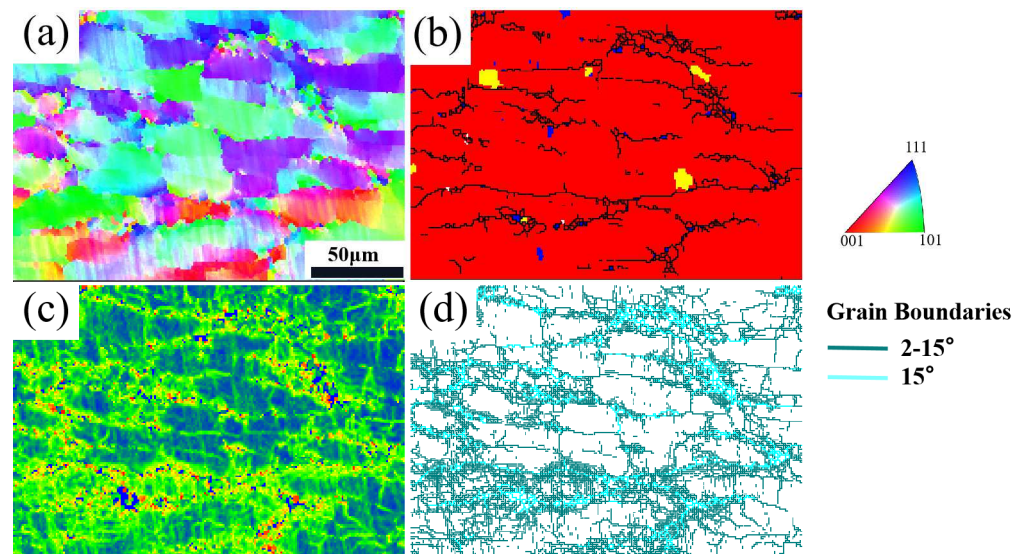


Figure 7. SEM and EBSD analysis of $(\text{NiAl})_{78}(\text{CoCrFe})_{16.5}\text{Cu}_{5.5}$ HEAs after compression at 800 °C: (a) IPF plot; (b) DefRex plot; (c) local dislocation misorientation; (d) corresponding distribution map of large- and small-angle grain boundaries: blue lines represent large-angle grain boundaries (greater than 15°); green line represents small-angle grain boundaries (2°–15°).

3.2.2. Wear Behavior

Figure 8 shows the hardness values of the unworn (adjacent to the worn surface) and worn surfaces after being tested at different temperatures. The hardness of the worn surface reaches its maximum value at 200 °C. However, the hardness of the unworn surface increases with the increase in test temperature. Figure 9 shows the wear friction coefficient and three-dimensional track morphology of $(\text{NiAl})_{78}(\text{CoCrFe})_{16.5}\text{Cu}_{5.5}$ HEAs after being tested at different temperatures. Table 3 shows the wear volume and wear rate of the HEAs. The relationship curve between the wear coefficient and sliding time at different temperatures is shown in Figure 9a. The wear coefficient curve of $(\text{NiAl})_{78}(\text{CoCrFe})_{16.5}\text{Cu}_{5.5}$ HEAs at 25–200 °C is relatively stable. As the temperature increases to 400 °C, the wear

coefficient curve of the alloy shows a trend of first increasing and then decreasing, the wear coefficient reaches its highest value (0.211) at 100 °C. It is related to the formation and destruction of the oxide film on the surface. In the early stage of testing, the contact surface continuously generates a more uniform oxide film than at low temperatures, providing good lubrication and minimizing the friction coefficient of the alloy. As the experiment progresses, the worn surface continuously oxidizes until an oxide glaze is formed. The bonding force between the oxide glaze and the alloy matrix is low, and it is easy to detach from the alloy surface under the cyclic load, which in turn increases the friction coefficient and the wear rate. Meanwhile, the average friction coefficient has a small change, ranging from 0.169 to 0.211. Figure 9b–e show the morphology of the alloy wear tracks. At room temperature (RT), the wear surface is smooth, and the specific wear rate first decreases and then increases with the increase in temperature throughout the entire test. At 400 °C, the wear rate increases to $1.77 \times 10^{-4} \text{ mm}^3/\text{Nm}$, the wear rate decreases to the lowest level of $7.05 \times 10^{-5} \text{ mm}^3/\text{N m}$ at 100 °C indicates a better anti-friction effect at 100 °C (Table 3).

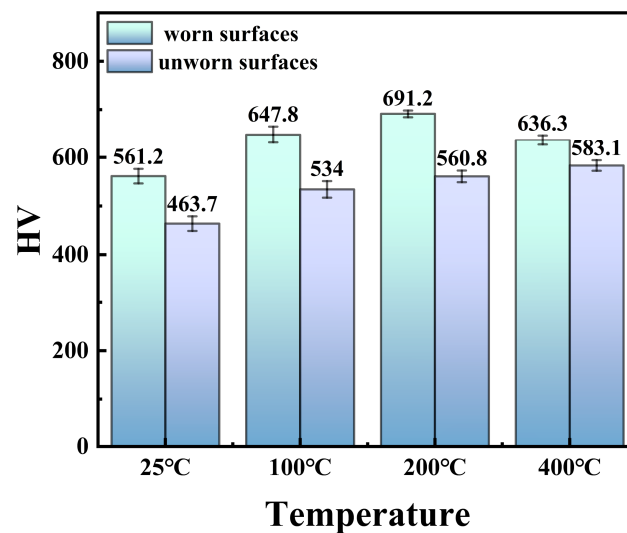


Figure 8. The hardness values of the unworn and worn surfaces of the $(\text{NiAl})_{78}(\text{CoCrFe})_{16.5}\text{Cu}_{5.5}$ HEAs after wear tests at different temperatures.

Figure 10 shows the wear track microstructure of the $(\text{NiAl})_{78}(\text{CoCrFe})_{16.5}\text{Cu}_{5.5}$ HEAs after wear tested from RT to 400 °C. There is a large number of debris and a small number of grooves on the worn surface (Figure 10a). This is caused by the detachment of debris from the worn surface and the transfer of adhering particles to the hard material surface, which will have a plowing effect on the soft metal during the wear process. However, the worn surface around the grooves is relatively intact. Therefore, its wear mechanism can be considered mild abrasive wear. As the temperature increases to 100 °C, the wear track microstructure becomes smoother and the shallow grooves decrease, as shown in Figure 10b. When the temperature continues to rise to 200 °C (Figure 10c), from the analysis results of the compression experiment in Section 3.2.1, it can be seen that the grain boundary strength of the alloy decreases with the increase in temperature. Therefore, hard abrasive debris is more likely to be pulled out of the matrix under the cyclic action of shear stress, exacerbating abrasive wear. When the temperature reaches 400 °C (Figure 10d), along the sliding direction, the worn surface exhibits a large number of plastic deformations plow shaped grooves and peeling pits. It indicates that further intensification of abrasive wear. The pits on the worn surface are usually related to adhesive wear, which means that the alloy undergoes slight softening at 400 °C, and hard abrasive particles are more likely to scratch the metal surface, leading to an increase in wear rate. Table 4 shows the EDS element content analysis at the worn surface after the wear test at different temperatures, indicating that oxidation occurred at all temperatures. The wear resistance of alloys is related to two factors: one is the formation rate and protective ability of the oxide film,

and the other is the detachment of hard abrasive particles. The research of Mei et al. [38] showed that with the increase in Cu content in AlTiVCuN alloys, the external diffusion of Cu promotes the formation of CuO oxides at high temperatures. In particular, at 600 °C, with the increase in Cu content, the friction coefficient decreased from 0.90 to 0.45, and then rebounded to 0.54, which is attributed to the reduction in the AlVO₄ phase and the increase in the CuO phase. The study by Liu et al. [15] also showed that Cu undergoes oxidation at high temperatures, and the generated wear-resistant CuO glaze layer can suppress adhesion wear. It indicates that after the detachment of small particles during sliding, the CuO film formed by adding Cu can promote the formation of the wear-resistant glaze layer, serving as a lubricant. Therefore, at 100 °C, the alloy achieves good balance and achieves good wear resistance. Thus, the worn surface is relatively smooth. As the temperature increases to 200 °C, the nano precipitates of (Cr, Fe)-rich elements in the Cu-rich region at the grain boundary aggregate and grow, the damage ability of hard particles exceeds the protective ability of the oxide film, resulting in a large number of plastic deformations plow shaped grooves and peeling pits on the worn surface. When the temperature reaches 400 °C, the thickness of the oxide film exceeds the critical value for detachment, resulting in severe oxidative wear. Furthermore, the further weakening of grain strength leads to the easier generation of hard particles. Therefore, the worn surface of the alloy exhibits severe abrasive wear and the highest wear rate.

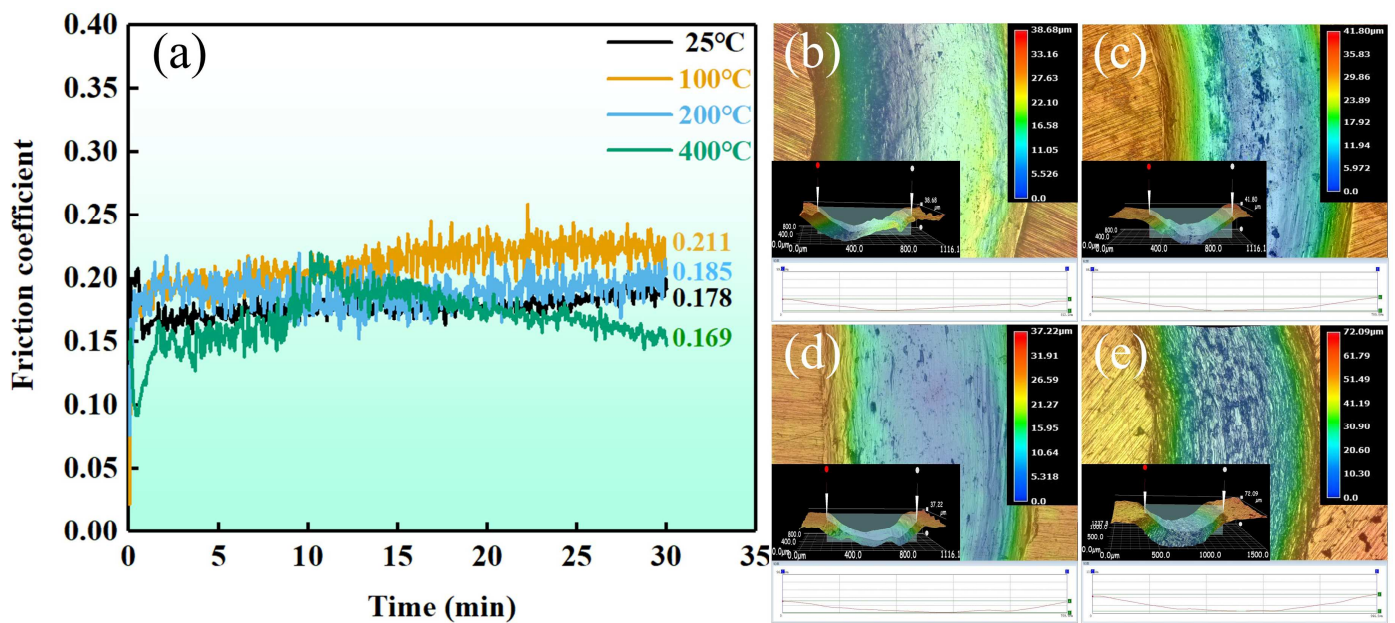


Figure 9. Friction and wear test results of (NiAl)₇₈(CoCrFe)_{16.5}Cu_{5.5} HEAs. (a) Wear coefficient curve at different temperatures; 2D cross-sectional profile of the worn surface and corresponding wear track: (b) RT; (c) 100 °C; (d) 200 °C; (e) 400 °C.

Table 3. Wear data of (NiAl)₇₈(CoCrFe)_{16.5}Cu_{5.5} HEAs at different temperatures.

| Temperature | Wear Volume (mm ³) | Specific Wear Rate (mm ³ /Nm) | Line Wear Rate (mm ³ /km) |
|-------------|--------------------------------|--|--------------------------------------|
| RT | 1.70 × 10 ⁻¹ | 7.53 × 10 ⁻⁵ | 0.38 |
| 100 °C | 1.59 × 10 ⁻¹ | 7.05 × 10 ⁻⁵ | 0.36 |
| 200 °C | 1.74 × 10 ⁻¹ | 7.69 × 10 ⁻⁵ | 0.39 |
| 400 °C | 4.00 × 10 ⁻¹ | 1.77 × 10 ⁻⁴ | 0.90 |

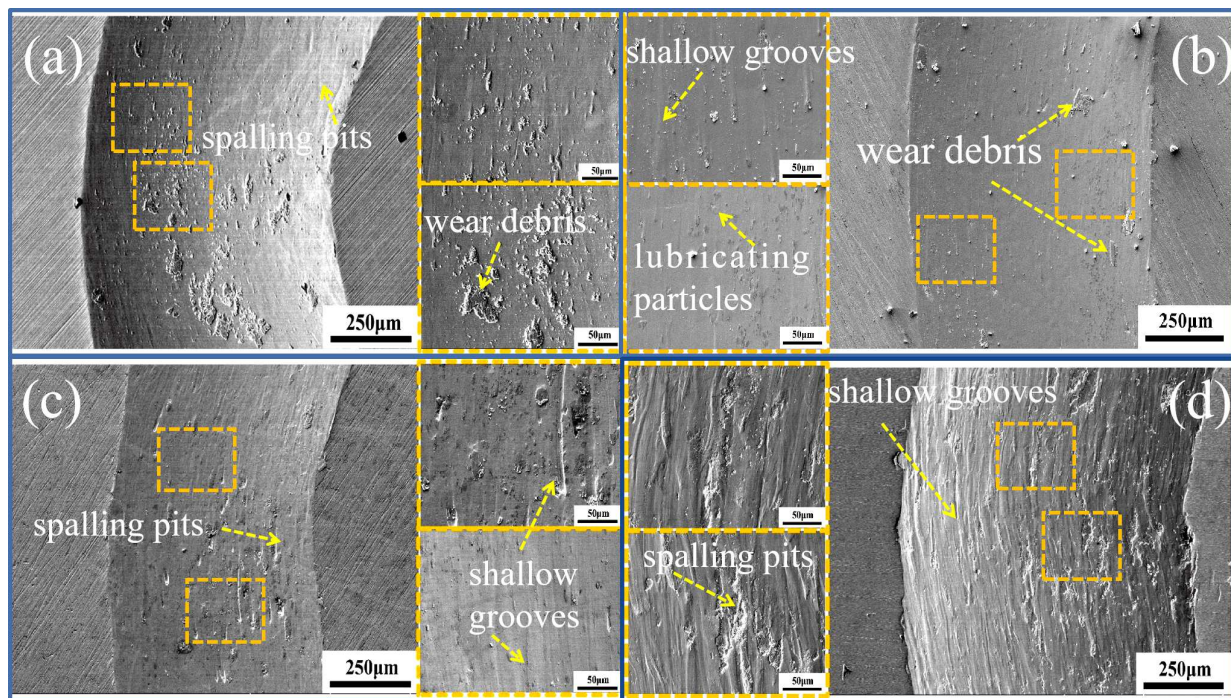


Figure 10. SEM of the wear tracks of $(\text{NiAl})_{78}(\text{CoCrFe})_{16.5}\text{Cu}_{5.5}$ HEAs. (a) RT; (b) 100 °C; (c) 200 °C; (d) 400 °C.

Table 4. EDS analysis of worn surface after wear test at different temperatures.

| Temperature | Al | Ni | Co | Cr | Cu | Fe | O |
|-------------|-------|-------|------|------|------|------|-------|
| 25 °C | 17.00 | 26.06 | 2.65 | 2.62 | 7.64 | 2.53 | 41.48 |
| 100 °C | 23.94 | 15.26 | 2.56 | 3.10 | 6.74 | 3.11 | 45.30 |
| 200 °C | 22.48 | 20.93 | 3.04 | 3.00 | 9.42 | 3.02 | 38.11 |
| 400 °C | 19.06 | 16.68 | 2.33 | 2.15 | 6.86 | 2.49 | 50.42 |

4. Conclusions

In this work, the $(\text{NiAl})_{78}(\text{CoCrFe})_{16.5}\text{Cu}_{5.5}$ HEA was designed based on Ni-Al alloy. The microstructure and phase composition were analyzed by XRD, SEM, EDS, and EBSD. Meanwhile, the mechanical properties and wear behavior at RT and high temperatures were studied. Based on the above analysis and results, the main conclusions are as follows:

1. $(\text{NiAl})_{78}(\text{CoCrFe})_{16.5}\text{Cu}_{5.5}$ HEAs have a dendritic structure, with the gray BCC phase as the matrix and the white FCC phase at the interdendritic. Spinodal decomposition structure appears in the matrix, and (Cr, Fe) rich nano-precipitation in the FCC phase.
2. The compression test shows that the $(\text{NiAl})_{78}(\text{CoCrFe})_{16.5}\text{Cu}_{5.5}$ HEAs exhibits good comprehensive properties at 600 °C. Dynamic recovery and recrystallization occur at 800 °C.
3. As the temperature of the wear test increases from RT to 400 °C, the surface grooves and plastic deformation of $(\text{NiAl})_{78}(\text{CoCrFe})_{16.5}\text{Cu}_{5.5}$ HEAs increase, while the peeling and debris decrease. The wear mechanism is mainly abrasive wear.

Author Contributions: Z.L.: Investigation and Software, Writing—original draft. X.W.: Conceptualization, Investigation, and Formal analysis, Writing—original draft. Y.H.: Investigation and Software. Z.X.: Investigation. Y.D.: Software. X.J.: Investigation, Methodology, and Writing—review and editing. X.Y.: Conceptualization, Formal analysis, Supervision, Funding acquisition, and Writing—review and editing. All authors have read and agreed to the published version of the manuscript.

Funding: This work was supported by the National Natural Science Foundation of China (Nos. 52301160, 52271106, 52171120), the Natural Science Foundation of Zhejiang Province (No. LZYZ3E050001).

Institutional Review Board Statement: Not applicable.

Informed Consent Statement: Not applicable.

Data Availability Statement: The authors confirm that the data supporting the findings of this study are available within the article.

Conflicts of Interest: The authors declare no conflict of interest.

References

1. Cantor, B.; Chang, I.T.H.; Knight, P.; Vincent, A.J.B. Microstructural development in equiatomic multicomponent alloys. *Mater. Sci. Eng. A* **2004**, *375*, 213–218. [\[CrossRef\]](#)
2. Senkov, O.N.; Wilks, G.B.; Miracle, D.B.; Chuang, C.P.; Liaw, P.K. Refractory high-entropy alloys. *Intermetallics* **2010**, *18*, 1758–1765. [\[CrossRef\]](#)
3. Zhang, Y.; Chen, M.; Yang, X. *Advanced Technology in High-Entropy Alloys*; Chemical Industry Publishing: Beijing, China, 2018.
4. Chang, Y.J.; Yeh, A.C. The evolution of microstructures and high temperature properties of $Al_xCo_{1.5}CrFeNi_{1.5}Ti_y$ high entropy alloys. *J. Alloys Compd.* **2015**, *653*, 379–385.
5. Tong, C.J.; Chen, Y.L.; Yeh, J.W.; Lin, S.J.; Chen, S.K.; Shun, T.T.; Chang, S.Y. Microstructure characterization of $Al_xCoCrCuFeNi$ high-entropy alloy system with multiprincipal elements. *Metall. Mater. Trans. A* **2005**, *36*, 881–893. [\[CrossRef\]](#)
6. Lu, Y.; Dong, Y.; Guo, S.; Jiang, L.; Kang, H.; Wang, T. A Promising New Class of High-Temperature Alloys: Eutectic High-Entropy Alloys. *Sci. Rep.* **2014**, *4*, 6200. [\[CrossRef\]](#)
7. Fan, Z.; Ru, L.B.; Jun, L.X.; Hui, W.; He, J.S.; Muhammed, N.; Li, W.X.; Yuan, W.; Ping, L.Z. Hydrogen embrittlement resistance of precipitation-hardened FeCoNiCr high entropy alloys. *Intermetallics* **2023**, *153*, 107800.
8. He, J.Y.; Wang, H.; Wu, Y.; Liu, X.J.; Mao, H.H.; Nieh, T.G.; Lu, Z.P. Precipitation behavior and its effects on tensile properties of FeCoNiCr high-entropy alloys. *Intermetallics* **2016**, *79*, 41–52. [\[CrossRef\]](#)
9. Jiang, S.; Wang, H.; Wu, Y.; Liu, X.; Chen, H.; Yao, M. Ultrastrong steel via minimal lattice misfit and high-density nanoprecipitation. *Nature* **2017**, *544*, 460–464. [\[CrossRef\]](#) [\[PubMed\]](#)
10. Sun, W.W.; Marceau, R.K.W.; Styles, M.J.; Barbier, D.; Hutchinson, C.R. G phase precipitation and strengthening in ultra-high strength ferritic steels: Towards lean maraging metallurgy. *Acta Mater.* **2017**, *130*, 28–46. [\[CrossRef\]](#)
11. Jin, X.; Zhou, Y.; Zhang, L.; Du, X.; Li, B. A new pseudo binary strategy to design eutectic high entropy alloys using mixing enthalpy and valence electron concentration. *Mater. Des.* **2018**, *143*, 49–55. [\[CrossRef\]](#)
12. Belov, N.A.; Alabin, A.N.; Eskin, D.G. Improving the properties of cold-rolled Al-6%Ni sheets by alloying and heat treatment. *Scr. Mater.* **2004**, *50*, 89–94. [\[CrossRef\]](#)
13. Osório, W.R.; Peixoto, L.C.; Canté, M.V.; Garcia, A. Electrochemical corrosion characterization of Al-Ni alloys in a dilute sodium chloride solution. *Electrochim. Acta* **2010**, *55*, 4078–4085.
14. Wang, Y.; Li, S.; Chen, F.; Yang, K.; Ge, G.; Tang, X. Unique dislocation loops distribution of AlCrFeNiTi_x eutectic high-entropy alloys under high-temperature ion irradiation. *J. Alloys Compd.* **2023**, *958*, 170373. [\[CrossRef\]](#)
15. Liu, D.; Yu, P.; Li, G.; Liaw, P.K.; Liu, R. High-temperature high-entropy alloys $Al_xCo_{15}Cr_{15}Ni_{70-x}$ based on the Al-Ni binary system. *Mater. Sci. Eng.* **2018**, *724*, 283–288.
16. Wang, L.; Shen, J.; Zhang, Y.; Guo, L.; Xu, H.; Fu, H. Microstructure evolution and room temperature fracture toughness of as-cast and directionally solidified novel NiAl-Cr (Fe) alloy. *Intermetallics* **2017**, *84*, 11–19. [\[CrossRef\]](#)
17. Misra, A.; Gibala, R. Room-temperature deformation behavior of directionally solidified multiphase Ni-Fe-Al alloys. *Metall. Mater. Trans. A* **1997**, *28*, 795–807.
18. Jin, X.; Zhou, Y.; Zhang, L.; Du, X.; Li, B. A novel Fe₂₀Co₂₀Ni₄₁Al₁₉ eutectic high entropy alloy with excellent tensile properties. *Mater. Lett.* **2018**, *216*, 144–146. [\[CrossRef\]](#)
19. Ishida, K.; Kainuma, R.; Ueno, N.; Nishizawa, T. Ductility enhancement in NiAl (B2)-base alloys by microstructural control. *Metall. Trans. A* **1991**, *22*, 441–446. [\[CrossRef\]](#)
20. Yu, Z.; Yan, Y.; Qiang, J.; Gao, W.; Wang, X.; Liu, X.; Du, W. Microstructure evolution and compressive property variation of $Al_xCoCrFeNi$ high entropy alloys produced by directional solidification. *Intermetallics* **2023**, *152*, 107749. [\[CrossRef\]](#)
21. Qiang, F.; Xin, S.; Guo, P.; Hou, H.; Wang, J.; Hou, W. Formation mechanism of interdiffusion layer and mechanical properties of Al_{0.6}CoCrFeNi high-entropy alloy/Ti composites. *J. Alloys Compd.* **2023**, *943*, 169151. [\[CrossRef\]](#)
22. Guo, J.T.; Cui, C.Y.; Chen, Y.X.; Li, D.X.; Ye, H.Q. Microstructure, interface and mechanical property of the DS NiAl/Cr (Mo, Hf) composite. *Intermetallics* **2001**, *9*, 287–297. [\[CrossRef\]](#)
23. Zaitsev, A.A.; Sentyurina, Z.A.; Levashov, E.A.; Pogozhev, Y.S.; Sanin, V.N.; Loginov, P.A.; Petrzhik, M.I. Structure and properties of NiAl-Cr (Co, Hf) alloys prepared by centrifugal SHS casting. Part 1—Room temperature investigations. *Mater. Sci. Eng. A* **2017**, *690*, 463–472. [\[CrossRef\]](#)
24. Wang, L.; Yao, C.; Shen, J.; Zhang, Y.; Wang, T.; Xu, H.; Zhang, G. Microstructures and compressive properties of NiAl-Cr (Mo) and NiAl-Cr eutectic alloys with different Fe contents. *Mater. Sci. Eng. A* **2019**, *744*, 593–603. [\[CrossRef\]](#)
25. Wang, L.; Su, Y.; Yao, C.; Huang, Y.; Shen, J.; Zhang, Y.; Liu, G.; Zhao, P.; Zhang, G. Microstructure and mechanical property of novel NiAl-based hypoeutectic/eutectic/hypereutectic high-entropy alloy. *Intermetallics* **2022**, *143*, 107476. [\[CrossRef\]](#)

26. He, J.Y.; Liu, W.H.; Wang, H.; Wu, Y.; Liu, X.J.; Nieh, T.G.; Lu, Z.P. Effects of Al addition on structural evolution and tensile properties of the FeCoNiCrMn high-entropy alloy system. *Acta Mater.* **2014**, *62*, 105–113. [[CrossRef](#)]
27. Zhang, X.; Li, B.; Zeng, L.; Yi, J.; Wang, B.; Hu, C.; Xia, M. Effect of Re addition on the microstructure and mechanical properties of AlCoCrFeNi_{2.1} eutectic high-entropy alloy. *Intermetallics* **2023**, *154*, 107808. [[CrossRef](#)]
28. Huo, W.; Zhou, H.; Fang, F.; Zhou, X.; Xie, Z.; Jiang, J. Microstructure and properties of novel CoCrFeNiTa_x eutectic high-entropy alloys. *J. Alloys Compd.* **2018**, *735*, 897–904. [[CrossRef](#)]
29. Chen, X.; Qi, J.Q.; Sui, Y.W.; He, Y.Z.; Wei, F.X.; Meng, Q.K.; Sun, Z. Effects of aluminum on microstructure and compressive properties of Al-Cr-Fe-Ni eutectic multi-component alloys. *Mater. Sci. Eng. A* **2017**, *681*, 25–31. [[CrossRef](#)]
30. Miracle, D.B.; Senkov, O.N. A critical review of high entropy alloys and related concepts. *Acta Mater.* **2017**, *122*, 448–511.
31. Hassan, M.A.; Yehia, H.M.; Mohamed, A.S.A.; El-Nikhaily, A.E.; Elkady, O.A. Effect of Copper Addition on the AlCoCrFeNi High Entropy Alloys Properties via the Electroless Plating and Powder Metallurgy Technique. *Crystals* **2021**, *11*, 540. [[CrossRef](#)]
32. Yuan, Y.; Hui, Q.Z.; Bo, R.H.; Min, L.W. Research progress on friction and wear properties of high entropy alloys. *Mater. Eng.* **2022**, *50*, 1–17.
33. Yan, G.X. Study on Solidification Structure and Properties of CoCrCuFeNi High Entropy Alloy. Master's Thesis, Jiangsu University of Science and Technology, Zhenjiang, China, 2014.
34. Ping, W.Y. Microstructure and Properties of AlCrFeCoNiCu System Multi principal Component Alloy and Its Composite Materials. Master's thesis, Harbin Institute of Technology, Harbin, China, 2009.
35. Yuan, L.; Min, C.; Xiang, L.Y.; Xiang, C. Microstructure and Mechanical Properties of Al_xCoCrCuFeNi Multi principal Component High Entropy Alloy. *Rare Met. Mater. Eng.* **2009**, *38*, 1602–1607.
36. Wei, S.; Na, L.X.; Tian, C.X.; Min, L.Z.; Hong, Z.Y.; Xiao, Y.Q.; Yv, W.C.; Chuang, D. Microstructure Evolution of Cu_x[Ni₃Fe₁] (x=4-12) Alloy. *J. Vac. Sci. Technol.* **2018**, *38*, 636–641.
37. Na, M.J.; Dong, W.T.; Na, W. Microstructure Evolution of FeCrNiMn Duplex High Entropy Alloys During High-Temperature Compression. *Rare Met. Mater. Eng.* **2022**, *51*, 4496–4501.
38. Mei, H.; Ding, J.C.; Zhao, Z.; Li, Q.; Song, J.; Li, Y.; Gong, W.; Ren, F.; Wang, Q. Effect of Cu content on high-temperature tribological properties and oxidation behavior of Al-Ti-V-Cu-N coatings deposited by HIPIMS. *Surf. Coat. Technol.* **2022**, *434*, 128–130. [[CrossRef](#)]

Disclaimer/Publisher's Note: The statements, opinions and data contained in all publications are solely those of the individual author(s) and contributor(s) and not of MDPI and/or the editor(s). MDPI and/or the editor(s) disclaim responsibility for any injury to people or property resulting from any ideas, methods, instructions or products referred to in the content.